Time evolution of vibrational temperatures in a CO_2 glow discharge as measured with infrared absorption spectroscopy

B.L.M. Klarenaar[1], R. Engeln[1], D.C.M. van den Bekerom[2],
M.C.M. van de Sanden[1,2], A.S. Morillo-Candas[3], O. Guaitella[3]

[1]Department of Applied Physics, Eindhoven University of Technology, 5600 MB Eindhoven, The Netherlands
[2]Dutch Institute for Fundamental Energy Research, 5600 HH Eindhoven, The Netherlands
[3]Laboratoire de Physique des Plasmas, Ecole Polytechnique-CNRS-Univ Paris-Sud-UPMC, 91128 Palaiseau, France

Vibrational temperatures of CO_2 are studied in a pulsed glow discharge by means of time-resolved *in situ* Fourier transform infrared (FTIR) spectroscopy, with a 10 µs temporal resolution. A method to analyze the infrared transmittance through vibrationally excited CO_2 is presented and validated on a previously published CO_2 spectrum, showing good agreement between fit and data. The discharge under study is pulsed with a typical duty cycle of 5-10 ms on-off, at 50 mA and 6.7 mbar. A rapid increase of the temperature of the asymmetric stretch vibration (T_3) is observed at the start of the pulse, reaching 1050 K, which is an elevation of 550 K above the rotational temperature (T_{rot}) of 500 K. After the plasma pulse, the characteristic relaxation time of T_3 to T_{rot} strongly depends on the rotational temperature. By adjusting the duty cycle, the rotational temperature directly after the discharge is varied from 530 K to 860 K, resulting in relaxation times between 0.4 ms and 0.1 ms. Equivalently, as the gas heats up during the plasma pulse, the elevation of T_3 above T_{rot} decreases strongly.

1. Introduction

Solar and wind energy play a crucial role in the transition of fossil fuels to renewable energy. However, due to the intermittent nature of these new energy sources, production and demand do not always coincide. One way of overcoming this intermittency problem is temporarily storing renewable energy in chemical bonds by making hydrocarbons from CO_2 [1]. A key step in this storage process is the efficient reduction of CO_2 to CO [2–4].

A promising route for energy efficient dissociation is through selective excitation of the asymmetric stretch vibration of CO_2 in a non-equilibrium plasma [5–7]. Studies on vibrational excitation of CO_2 are mostly done in the field of CO_2 lasers, reporting vibrational temperatures which are elevated with respect to the translational temperature [8–11]. These measurements are performed in continuous glow discharges, determining vibrational excitations depending on e.g. gas composition, pressure, plasma current, and reduced electric field. Time-resolved measurements on pulsed CO_2 discharges are only rarely performed [12]. However, such measurements could give detailed insight in the time evolution of vibrational state densities, including excitation and relaxation times, and can be used for comparison and validation of (rate constants used in) kinetic models of CO_2 discharges.

Possible methods for detecting vibrational state densities include spontaneous Raman scattering [13, 14] and coherent anti-Stokes Raman scattering (CARS) [15, 16]. These spatially and time-resolved techniques are well suited to determine Raman active vibrations, like those of CO, O_2, and N_2. For CO_2, however, only the symmetric stretching mode is Raman active [17], hence densities of the asymmetric stretching mode (and bending mode) cannot be determined. On the other hand, these modes are strongly IR active [17] and therefore it is possible to determine the vibrational state densities using IR emission spectroscopy [13, 18, 19]. However, reabsorption of emitted IR radiation by the optically thick CO_2 makes it particularly difficult to determine densities deeper inside the discharge.

Using IR absorption spectroscopy, one is able to accurately determine vibrational state densities inside the plasma over several orders of magnitude. To this purpose, tunable diode lasers (TDL) are used as an IR source to determine densities in CO_2 lasers [9, 11]. Although TDLs can scan mode hop free only very narrow frequency ranges (in the order of single wavenumbers), a well selected range can contain absorption lines of multiple vibrational levels. Unfortunately, the nature of operation prohibits easy implementation of time-resolved measurements. The quickly pulsed and chirped (several wavenumbers) quantum cascade laser (QCL) is a good alternative, but has its own challenge in the form of the peak-distorting rapid passage effect [20].

To combine the ability of doing time-resolved measurements with measuring IR absorption over a wider wavenumber range, we use *in situ* Fourier transform infrared (FTIR) spectroscopy. Rivallan et al. [12] already showed its suitability to detect time-resolved absorption lines in a glow discharge using an air/CO_2 mixture. We exploit the homogeneity of the positive column of the glow discharge [21] to study the time evolution of the vibrational temperatures of CO_2 and CO (formed in the discharge), during plasma ignition, development to steady state, and during relaxation directly after

the plasma pulse.

Although the three vibrational modes of CO_2 are not all IR active, they all affect the absorbance spectrum, hence all modes are taken into account [9, 10]. Quantum numbers ν_1, ν_2, and ν_3 are used to represent the symmetric stretch, doubly degenerate bending, and asymmetric stretch mode, respectively. Additionally, the contribution of ν_2 to the angular momentum is described using number l_2. Since the energy of one ν_1 quantum and two ν_2 quanta is almost equal, and their symmetry is the same if ν_2 does not contribute to the angular momentum, there is a strong Fermi resonance between states of the form $(\nu_1, \nu_2^{l_2}, \nu_3)$ and $((\nu_1 - 1), (\nu_2 + 2)^{l_2}, \nu_3)$ [22–24].

2. Experimental methods

The experimental setup is schematically shown in Fig. 1a. The plasma reactor is made of Pyrex and is cylindrically shaped with an inner diameter of 2 cm and a length of 23 cm, with BaF_2 windows at the sides. The electrodes and gas in- and outlet are both 17 cm apart. A 50 mA DC current is achieved by connecting a 50 kΩ resistor in series and applying 4.0 kV (2.5 kV over the resistor and 1.5 kV over the reactor). A high-voltage probe (LeCroy, *PPE 20kV*) and an oscilloscope (LeCroy, *LT584M*) are used to monitor the voltage. The power supply is triggered using a pulse generator (TTi, *TGP110*), resulting in square pulses with rise and fall times in the order of a couple µs. The plasma is pulsed with a typical time of 5-10 ms on-off. A basic trigger scheme is shown in Fig. 1b.

The incoming gas consists of pure CO_2 (Air Liquide, *Alphagaz 1*) and the gas flow is controlled at 7.4 sccm using a mass flow controller (Bronkhorst, *F-201CV*). Pressure is maintained at 6.7 mbar with a scroll pump (Edwards, *XDS5*) and a manual valve, while the pressure is measured using a pressure gauge (Pfeiffer, *CMR 263*). With the reactor dimensions as mentioned earlier, the gas residence time is in the order of seconds.

The reactor is positioned in the sample compartment of an FTIR spectrometer (Bruker, *Vertex 70*), shown in Fig. 1(a). Time resolved measurements are performed by operating the spectrometer in the step-scan mode. In this mode, the interferometer assumes a position, relaxes for 60 ms, and awaits a trigger signal, e.g. from a pulse generator. After receiving a trigger, the DC signal of the IR detector (MCT) is repetitively read out with a period of 10 µs, hence, 1100 repetitions result in a measured time period of 11 ms. Four trigger series are averaged per interferometer position (53, 323 in total), whereafter the interferometer moves to the next position and the procedure is repeated, building a 2D interferogram. Fourier transforming the

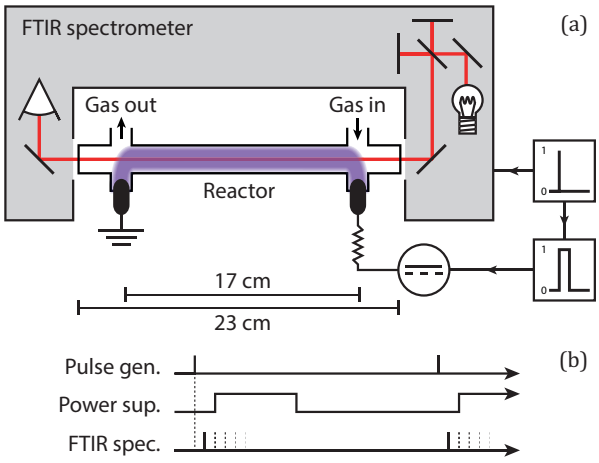

Fig. 1: (a) The FTIR spectroscope, including the plasma reactor, positioned in the sample compartment. A pulse generator is used to simultaneously trigger the step-scan mode of the spectroscope and the square DC pulse for the plasma. The trigger scheme is shown in (b).

interferogram gives a time-resolved intensity spectrum with a 10 µs resolution and a spectral resolution of 0.2 cm^{-1}. A trigger scheme including the pulse generator, the gating of the power supply of the reactor, and the read-out by the IR detector is shown in Fig. 1(b).

The infrared light that reaches the detector is a combination of three contributions:

- Light coming from the IR source of the spectrometer.
- Spontaneous emission of vibrationally excited molecules inside the plasma that is directly emitted towards the detector.
- Spontaneous emission that first enters the interferometer and is reflected back through the reactor.

To be able to study the light absorption from the IR source through the reactor, the intensity spectrum should be corrected for other spectrally resolved contributions. Light that is directly emitted from the plasma towards the detector only induces an interferogram offset, which is not apparent after Fourier transformation. On the other hand, plasma emission that is reflected by the interferometer is spectrally resolved: it depends on the mirror position of the interferometer which frequencies are reflected. The intensity spectrum should be corrected for this and accordingly a time-resolved measurement is performed while blocking all light from the IR source, revealing only the plasma emission.

After subtracting the emission from the intensity spectrum, the time-resolved transmittance is calculated by dividing the remainder by the spectral profile of the IR source. This common background is taken after purging the reactor with nitrogen and operating the FTIR spectrometer in its

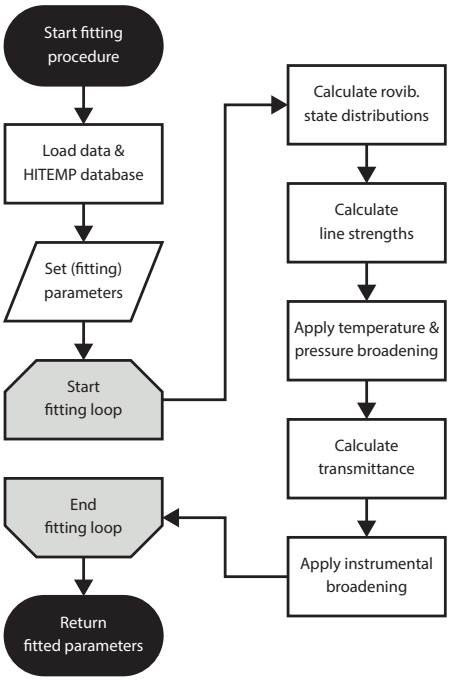

Fig. 2: A calculation diagram of the developed algorithm to compute and fit non-equilibrium infrared transmittance spectra. The left hand column represents the preparation of the calculation, including the users choice (parallelogram) of to be fitted parameters. The fit loop (hexagons) that involves the calculation of the spectra, is elaborated in the right hand column.

conventional mode. The spectral region between 1975 cm^{-1} and 2400 cm^{-1} contains lines of both CO and asymmetric-stretch transitions of CO_2 and is analyzed using the fitting algorithm, discussed in the next section.

3. Computational algorithm

3.1. Database and fitting parameters

Due to the discharge conditions, the measured FTIR spectra result from infrared absorption by a molecular population which is not in thermal equilibrium. To be able to accurately analyze these spectra, an algorithm has been developed to calculate and fit these non-equilibrium infrared absorption spectra. The basic flowchart for the algorithm can be seen in Fig. 2.

The algorithm makes use of the HITEMP-2010 database [25], which contains transition energies, Einstein A coefficients, broadening constants, etc., of a wide variety of molecules. Transition data for CO_2 is available up to $\nu_3 = 6 \rightarrow 7$, while vibrational transitions of CO are documented as far as $\nu_{CO} = 14 \rightarrow 15$. Transitions of both these vibrational quanta (i.e. $(\nu_1, \nu_2^{l_2}, \nu_3) \rightarrow (\nu_1, \nu_2^{l_2}, \nu_3 + 1)$ and $(\nu_{CO}) \rightarrow (\nu_{CO} + 1)$) are present in the region of interest of 1975–2400 cm^{-1}. The rotationless transition energies of the ground state to the first level are centered around 2349 cm^{-1} and 2143 cm^{-1}, for CO_2 and CO, respectively [22, 26]. Depending on the measurement conditions, the CO and CO_2 lines will partially overlap. Hence, in an accurate analysis CO should be included.

Table 1: List of fitting parameters, including symbol, description, and guess value for the fit.

Symbol	Description	Guess
T_{rot}	Rotational temperature	600 K
$T_{1,2}$	$\nu_{1,2}$ temperature of CO_2	600 K
T_3	ν_3 temperature of CO_2	600 K
T_{CO}	Vib. temperature of CO	600 K
c_{T_t}	Thermal variable	0.1
α	CO_2 conversion factor	0.3
p	Pressure	Var.

Before continuing to calculate a spectrum, several parameters have to be set. Table 1 shows the parameters that are included in the fit. The rotational temperature T_{rot} is assumed to be the same for molecules of CO_2 and CO. The vibrational temperature, however, is split into different parameters. Since modes ν_1 and ν_2 of CO_2 are Fermi coupled, they are described with one temperature, $T_{1,2}$ [22]. For the asymmetric stretch mode T_3 is used, and T_{CO} is used for the vibrational temperature of CO.

Absorption spectroscopy is a line-of-sight technique, i.e. under the present experimental conditions measured spectra result from absorption over the full length of the reactor. As Fig. 1 shows, this length is not completely filled by the discharge, resulting in two greatly different temperature regions: thermal gas and non-thermal plasma. Therefore, f_t, the volume fraction of thermal gas is introduced. For the analysis in this study, this fraction is fixed at $(23\,cm - 17\,cm)/23\,cm \approx 0.26$, based on the length of the reactor and the positioning of the electrodes. T_t describes the translational energy and rovibrational densities in this volume, having a lower and upper limit of 273 K and T_{rot}, respectively, and is fitted using thermal variable c_{T_t} $(0 \leq c_{T_t} \leq 1)$:

$$T_t = c_{T_t} \cdot (T_{rot} - 273) + 273. \quad (1)$$

To calculate the number densities of molecules in the thermal and non-thermal region, n_t and n_{nt}, respectively, it is assumed that the pressure in both parts is equal, p. Additionally, in the non-thermal part the translational temperature is assumed to be equal to the rotational temperature. Using the ideal gas law results in Eqs. (2) and (3):

$$n_{t,eff} = f_t n_t = f_t \frac{p}{k_B T_t}, \quad (2)$$

$$n_{nt,eff} = (1 - f_t) n_{nt} = (1 - f_t) \frac{p}{k_B T_{rot}}, \quad (3)$$

where k_B is the Boltzmann constant and n_{LS} is the effective number density over the line of sight of the absorption measurement.

The molecular fractions of CO_2 and CO are assumed to be the same in the thermal and non-thermal part and are calculated using the conversion factor α, defined as

$$\alpha = \frac{[\mathrm{CO}]}{[\mathrm{CO}] + [\mathrm{CO_2}]}, \tag{4}$$

where $[CO_2]$ and [CO] are the molecular concentrations of CO_2 and CO, respectively. Other than CO_2 and CO, IR transmittance spectra reveal only insignificant amounts of O_3 (O_2 is not IR active). Therefore, following dissociation reaction

$$2\mathrm{CO_2} \rightarrow 2\mathrm{CO} + \mathrm{O_2}, \tag{5}$$

it is assumed that for every two CO molecules, one O_2 molecule is present in the reactor. This results in Eqs. (6) and (7) for the molecular fractions of CO_2 and CO, accordingly:

$$f_{\mathrm{CO_2}} = \frac{1-\alpha}{1+\alpha/2} \tag{6}$$

$$f_{\mathrm{CO}} = \frac{\alpha}{1+\alpha/2}. \tag{7}$$

To calculate the molecular number densities of thermal and non-thermal CO_2 and CO, these fractions should be multiplied by Eqs. (2) and (3).

3.2. Calculating the spectrum

Calculate rovibrational state distributions

After defining the fitting parameters, the first step in constructing a transmittance spectrum is calculating the thermal and non-thermal rovibrational state distributions. For this, it is assumed that energies of rotational levels and energies of different vibrational modes are independent. In literature, this is a widely used approximation, though it should be noted that it becomes less accurate for higher vibrational states [9, 27–29].

The population N_s of state s, having rotational state J and vibrational state(s) ν_i, can then be calculated, using:

$$N_s = N\phi_{\mathrm{rot},J}\prod_i \phi_{\mathrm{vib},\nu_i}. \tag{8}$$

Here, N is the total number of molecules per unit volume and i is an index for vibrational modes (i.e. 1, 2, and 3 for CO_2, while CO only has one vibrational mode). $\phi_{\mathrm{rot},J}$ and $\phi_{\mathrm{vib},\nu_i}$ are the fraction of molecules in the rotational state and vibrational state(s) of s, respectively.

Table 2: List of values for B (cm^{-1}), D (10^{-6} cm^{-1}), and H (10^{-12} cm^{-1}) for CO_2 and CO, calculated from [23, 32, 33].

Isotopologue	B	D	H
$^{12}C^{16}O_2$ [23]	0.39022	0.1333	0.0090
$^{13}C^{16}O_2$ [23]	0.39024	0.1332	0.0090
$^{16}O^{12}C^{18}O$ [23]	0.36819	0.1187	0.0075
$^{16}O^{12}C^{17}O$ [23]	0.37862	0.1255	0.0082
$^{12}C^{16}O$ [32]	1.9225	6.121	5.7
$^{13}C^{16}O$ [33]	1.8380	5.593	5.5
$^{12}C^{18}O$ [33]	1.8310	5.550	4.9

ϕ_{rot} is calculated assuming a Boltzmann distribution:

$$\phi_{\mathrm{rot},J} = \frac{g_{\mathrm{rot},J}}{Q_{\mathrm{rot}}}\exp\left(-\frac{hcE_{\mathrm{rot},J}}{k_B T_{\mathrm{rot}}}\right), \tag{9}$$

where h, c, and k_B are Planck's constant, the speed of light, and the Boltzmann constant, respectively. The energy $E_{\mathrm{rot},J}$ of rotational state J is calculated using the rotational constant B, centrifugal distortion constant D, and third order correction factor H as listed for all isotopologues of CO_2 and CO that are included in the algorithm, in Table 2. The rotational degeneracy $g_{\mathrm{rot},J}$ is a product of the factor $(2J+1)$ and a rotational-state-dependent and -independent weight, which can be found for different isotopologues in [30]. The rotational partition sum Q_{rot} is calculated such that ϕ_{rot} is normalized and its sum over all J is equal to one, as done in McDowell *et al.* [31].

Going back to Eq. (8), in the plasma a Treanor distribution is assumed for vibrational states, which Dang *et al.* [9] experimentally confirmed to be accurate in very similar glow discharges [34]. $\phi_{\mathrm{vib},\nu_i}$ then becomes:

$$\phi_{\mathrm{vib},\nu_i} = \frac{g_{\mathrm{vib},\nu_i}}{Q_{\mathrm{vib},i}}\times \exp\left(-\frac{hc}{k_B}\left(\nu_i\frac{G_{1,i}}{T_i} - \nu_i(\nu_i-1)\frac{\omega_e x_{e,i}}{T_{\mathrm{rot}}}\right)\right). \tag{10}$$

Here, g_{vib,ν_i} is the degeneracy of vibrational mode ν_i (for CO_2 $g_{\mathrm{vib},\nu_1} = g_{\mathrm{vib},\nu_3} = 1$, $g_{\mathrm{vib},\nu_2} = \nu_2+1$ and for CO $g_{\mathrm{vib},\nu_{\mathrm{CO}}} = 1$). $G_{1,i}$ is the energy spacing between the ground and first vibrational level, and $\omega_e x_{e,i}$ is the anharmonicity, listed in Table 3 for the isotopologues of CO_2[1] and CO that are included in the algorithm. Cross terms are not taken into account, since the vibrational modes are treated as independent. It is inherent to the Treanor distribution that

[1] For values of ν_2 a full contribution of angular momentum is included (i.e. $l_2 = \nu_2$). Furthermore, Fermi resonance between $(\nu_1, \nu_2^{l_2}, \nu_3)$ and $((\nu_1-1), (\nu_2+2)^{l_2}, \nu_3)$ induces a Fermi-level dependent energy shift which is not included in the listed values for ν_1. In the fitting algorithm, these shifts are calculated as described in [23, 24].

Table 3: List of values for G_1 and $\omega_e x_e$ (both in cm^{-1}) for CO_2[1] and CO, calculated from [23, 32, 33].

Isotopologue	Mode	G_1	$\omega_e x_e$
$^{12}C^{16}O_2$ [23]	ν_1	1333.93	2.93
	ν_2	667.47	−0.38
	ν_3	2349.16	12.47
$^{13}C^{16}O_2$ [23]	ν_1	1334.32	2.93
	ν_2	648.63	−0.37
	ν_3	2283.49	11.71
$^{16}O^{12}C^{18}O$ [23]	ν_1	1295.72	2.76
	ν_2	662.47	−0.39
	ν_3	2332.15	12.34
$^{16}O^{12}C^{17}O$ [23]	ν_1	1296.04	2.76
	ν_2	643.44	−0.36
	ν_3	2265.98	11.59
$^{12}C^{16}O$ [32]	ν_{CO}	2143.24	13.29
$^{13}C^{16}O$ [33]	ν_{CO}	2096.03	12.70
$^{12}C^{18}O$ [33]	ν_{CO}	2092.09	12.65

the harmonic part is scaled with vibrational temperature T_i ($= [T_{1,2}, T_{1,2}, T_3, T_{CO}]$ for $i = [1, 2, 3, CO]$), while the anharmonic part is scaled with the translational, or rotational temperature T_{rot}. When for thermal gas $T_i = T_{rot} = T_t$, Eq. (10) reduces back to a Boltzmann distribution.

Similar to the rotational partition sum, the partition sum of vibrational modes $Q_{vib,i}$ is determined such that the fractions ϕ_{vib,ν_i} are normalized:

$$\sum_{\nu_i=0}^{\nu_{i,max}} \phi_{vib,\nu_i} = 1. \quad (11)$$

Here, $\nu_{i,max}$ is the maximum vibrational state taken into account ($\nu_{i,max} = [40, 70, 30, 35]$ for $i = [1, 2, 3, CO]$), chosen such that all levels up to at least 6 eV are included in the calculation.

Calculate line strengths

The next step is the calculation of the line strength, starting from the Einstein A coefficient A_{ul} for spontaneous emission from upper state u to lower state l. This coefficient is listed in the HITEMP database. The line strength S_j of transition j can be calculated as follows [30]:

$$S_j = \frac{I_a g_{rot,u} A_{ul}}{8\pi c \tilde{\nu}_j^2} \left(\frac{N_l}{g_l N} - \frac{N_u}{g_u N} \right), \quad (12)$$

where I_a is the fractional abundance of the isotopologue as listed in [30], $\tilde{\nu}_j$ is the transition energy as listed in the HITEMP database, and g_l and g_u are the total rovibrational degeneracy of the lower and upper state, respectively[2]. Eq. (8) is now used to compute the lower and upper state densities, N_l and N_u, respectively.

Although Eq. (12) is derived using the relations between spontaneous emission and stimulated emission and absorption coefficients under the assumption of thermal-equilibrium black-body radiation, it is also valid in situations where there is no thermal equilibrium [35].

Apply temperature and pressure broadening

The HITEMP database lists for each line a self- and air-broadened half-width, as well as a CO_2-broadened half-width for CO. Broadening due to pressure from other molecular species is approximated as if it were from air. The Lorentzian pressure broadening profile is convolved with the Gaussian shaped Doppler broadening and multiplied by the line strength S_j. This results in a Voigt-shaped cross section $\sigma_j(\tilde{\nu})$, unique for every line j [36, 37]. The Voigt shape is applied using the empirical expression by Whiting [37, 38].

Calculate transmittance

The transmittance $T_{\tilde{\nu}}$ is calculated using the Beer-Lambert law [28]:

$$T_{\tilde{\nu}}(\tilde{\nu}) = \prod_{n=n_{t,eff}}^{n_{nt,eff}} \prod_{f=f_{CO}}^{f_{CO_2}} \exp\left(-Lnf \sum_{j=1}^{j_{max}} \sigma_j(\tilde{\nu}) \right), \quad (13)$$

where L is the length of the reactor. The transmittance is constructed from a product of four exponents, i.e. the contributions of thermal and non-thermal CO_2 and CO.

Apply instrumental broadening

In the last step the broadening of the instrument is applied. The final transmittance is obtained by convolving $T_{\tilde{\nu}}$ with the instrumental line shape of the FTIR. A three-term Blackman-Harris is used as the apodization function for the Fourier transform, resulting in a spectral line shape which can be very well approximated by a Gaussian [39]. For spectrometer settings as used in this study, the full-width at half-maximum of this Gaussian is determined to be 0.27 cm^{-1}.

3.3. Validation of the algorithm

The computational algorithm is tested on non-thermal data, obtained from literature. Dang *et al.* [9] performed IR absorption measurements on a glow discharge in a gas mixture of 10% CO_2, 38% N_2, and 52% He at a pressure of 20 mbar and a plasma current of 10 mA. They used a diode as an

[2] It would be physically accurate to replace the rotational degeneracy $g_{rot,u}$ in Eq. (12) by the total degeneracy g_u. However, $g_{rot,u}$ is used because of how A_{ul} is determined in the HITEMP database [30].

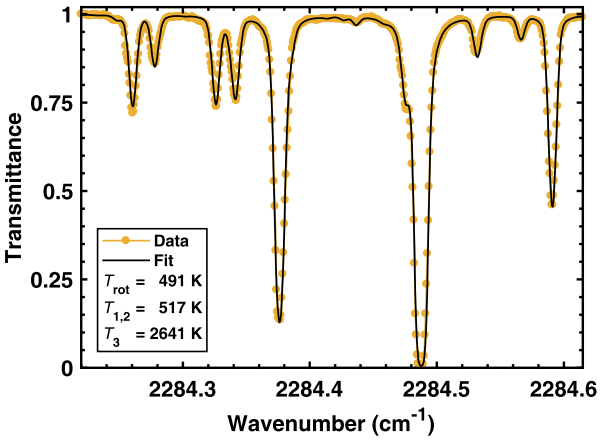

Fig. 3: A fit, using the algorithm, on CO_2 data from Dang *et al.* [9] Transmission data is digitally extracted from the article and divided by an artificial background.

infrared source, resulting in a very narrow scanning range from 2284.2 cm^{-1} to 2284.6 cm^{-1}. The transmission graph they provided in [9] has been digitally extracted and divided by an artificial background, resulting in the transmittance in Fig. 3. All features in the spectrum originate from transitions in CO_2, since N_2 and He are not IR active, while CO, which is formed in the plasma, is not active in this wavenumber region.

The spectrum is fitted using the algorithm, not including any thermal gas, nor instrumental broadening, since this broadening is not significant in regard to temperature and pressure broadening when using a diode as an IR source. The best fit, which is shown in Fig. 3, is obtained with $T_{\mathrm{rot}} = 491$ K, $T_{1,2} = 517$ K, and $T_3 = 2641$ K. Although Dang *et al.* do not provide temperatures for this measurement, a T_3 elevation with respect to T_{rot} of 2150 K is comparable to those under similar conditions listed in [9], i.e. between 1500 K and 2500 K.

4. Results

4.1. Adding thermal-volume fraction

Fig. 4 shows a measurement taken at 2 ms in the discharge of a 5-10 ms on-off duty cycle of 50 mA at 6.7 mbar. The spectrum is fitted once with f_{t} set to 0 and once with the default value of 0.26, in order to illustrate the effect of adding a thermal-volume fraction to the calculation of the transmittance spectra. Both fits are respectively shown in panels (a) and (b), including residuals.

The effect of adding thermal gas is most visible around 2349 cm^{-1}, which is the central wavenumber of the line structure of the $(0, 0^0, 0) \rightarrow (0, 0^0, 1)$ transition of $^{12}C^{16}O_2$. In panel (a), symmetrically around this point an oval shape indicates a discrepancy between data and fit. This discrepancy is further exposed in the residual. The general shape of the residual is typical for a transmittance spectrum of CO_2 in the vibrational ground state, which is fitted with a too high rotational temperature.

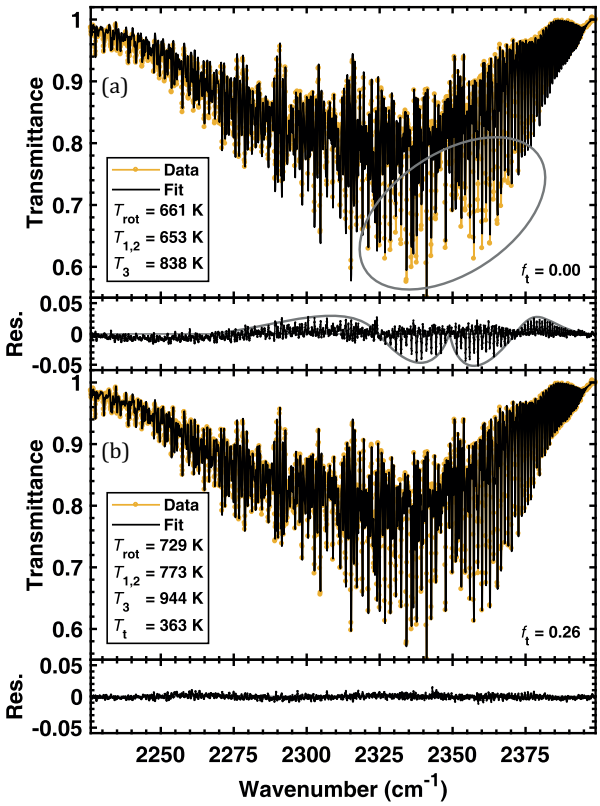

Fig. 4: Two fits on the same CO_2 and CO data at 2 ms in the discharge with a 5-10 ms on-off duty cycle at 50 mA and 6.7 mbar. In panel (a) $f_{\mathrm{t}} = 0$, assuming a non-thermal population over the whole reactor, while in (b) $f_{\mathrm{t}} = 0.26$. The residual is shown on the same scale as the data.

In panel (b) this discrepancy has disappeared by adding to the fitting conditions that 26% of the gas in the reactor volume is thermal. The temperature of the thermal gas fraction is fitted at 363 K, while the rotational temperature of the non-thermal fraction increased from 661 K in (a) to 729 K in (b). Also $T_{1,2}$ and T_3 from the fitted spectra significantly increase from (a) to (b). These temperatures largely represent the ratio of the ground state density over the density of vibrationally excited states. At temperatures below 400 K thermally distributed CO_2 and CO mainly populate the ground state (82% and 99.96%, respectively). Hence, if the thermal volume is not included in the fitting model, the ground-state density in the non-thermal part apparently increases, lowering the fitted vibrational temperatures.

4.2. Fitting a time-resolved series

Fig. 5 shows the time-resolved measurement series at 6.7 mbar, 50 mA, and a 5-10 ms on-off se-

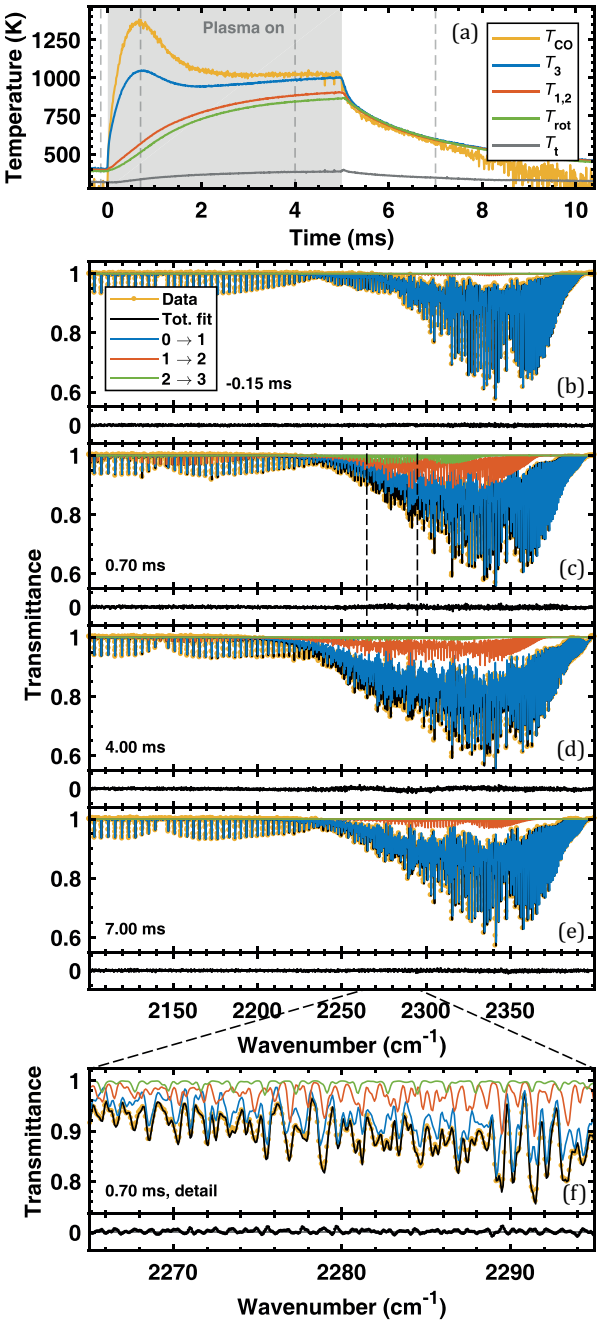

Fig. 5: A time-resolved measurement series at a pressure of 6.7 mbar, plasma current of 50 mA, and a 5-10 ms on-off sequence. Panel (a) shows the fitted temperatures versus time. The dashed lines indicate the time points for which the fit on the data is displayed in panels (b) to (e). Residuals are shown below each panel. CO_2 and CO lines are mostly located at energies respectively larger and smaller than 2235 cm^{-1}. Contributions to the fit corresponding to transitions of ν_3 or ν_{CO} of $0 \rightarrow 1$, $1 \rightarrow 2$, and $2 \rightarrow 3$ are shown separately. Panel (f) shows a detail of panel (c).

quence. In panel (a) the fitted T_{rot}, $T_{1,2}$, T_3, T_{CO}, and T_t are plotted versus time. The grey section marks the plasma-on phase. Panels (b) to (e) represent examples of the fitted spectra at the time points that are indicated by the dashed vertical lines in panel (a). The total fits are shown in black, while the colored spectra represent the individual contributions of transitions of the forms $(\nu_1, \nu_2^{l_2}, \nu_3) \rightarrow (\nu_1, \nu_2^{l_2}, (\nu_3 + 1))$ and $(\nu_{CO}) \rightarrow (\nu_{CO} + 1)$. The residual of the total fit is included below each panel. Lines at energies larger than 2235 cm^{-1} mainly belong to CO_2, while lines of CO are mostly located below this energy. Panel (f) shows a detail of panel (c).

Panel (a) shows the temperature behavior as a function of time, and starts right before the plasma is switched on, with all temperatures of the non-thermal part in equilibrium at 400 K (T_{CO} is not sensitive around this temperature and is stuck at the lower fitting boundary of 273 K). At this temperature ν_3 state densities are very low, and accordingly, in panel (b) hardly any lines are visible for $\nu_3 > 0$. Hereafter, T_3 and T_{CO} increase rapidly until a maximum is reached at 0.70 ms. In panel (c) this is seen as an increase of lines coming from $\nu_3 = 1 \rightarrow 2$ and $2 \rightarrow 3$, and $\nu_{CO} = 1 \rightarrow 2$. Continuing in time, T_{rot} and $T_{1,2}$ follow a similar growth and all temperatures of the non-thermal part develop towards a non-thermal equilibrium between 850 K and 1050 K. In panel (d), at 4.00 ms, the CO_2 and CO spectra become wider as a result from an increased density of higher rotational, ν_1, and ν_2 states. At 5.00 ms the plasma turns off and the thermal-volume part equilibrates within tens of µs. In panel (e) a transmittance spectrum is shown at 7.00 ms, with all temperatures half-way relaxed towards the initial conditions in panel (b). The thermal temperature T_t only increases and decreases slightly during and after the pulse, staying between 300 K and 400 K.

Before further discussion on the fitted temperatures, the fit of the calculated spectra to the data is studied in more detail. To this purpose, a parameter scan of several fitting parameters is performed while calculating the reduced chi-squared, χ^2_{red} [40]:

$$\chi^2_{red} = \frac{1}{N-n} \sum_{i=1}^{N} \frac{(O_i - F_i)^2}{\sigma^2}. \qquad (14)$$

Here, N is the number of wavenumber points, n is the number of fitting parameters, and O and F is the observed and fitted transmittance, respectively. σ^2 is the variance of the noise on the data, calculated from a wavenumber region without spectral activity. In short, χ^2_{red} represents the normalized ratio of the variance of the residual of the fit to the variance of the noise on the data. The closer χ^2_{red} is to 1, the better the model fits the data, though $\chi^2_{red} < 1$ means that the model is overfitting.

In Fig. 6 χ^2_{red} is plotted for parameter scans of T_{rot}, $T_{1,2}$, T_3, and T_{CO} for the time points of Fig. 5(b)–(e). The plots are constructed by fitting the data while fixing one of these temperatures at

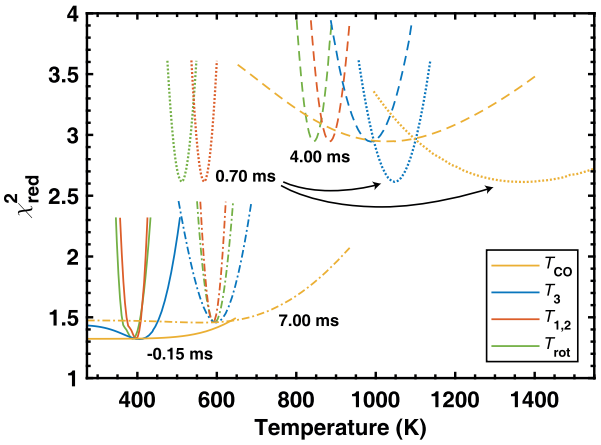

Fig. 6: The reduced chi-squared for varying T_{rot}, $T_{1,2}$, T_3, and T_{CO} individually. The same time points are used as in Fig. 5. Time points are grouped in line style, while color indicates the tested temperature.

various values (horizontal axis) and calculating χ^2_{red} of the resulting fit (vertical axis). In this way, χ^2_{red} forms a shape with its minimum at the original fit outcome, generally in the shape of a parabola; a higher or lower temperature respectively results in too strong or too weak peaks for vibrationally excited species. However, at -0.15 ms and 7.00 ms T_{CO} as well as T_3 at -0.15 ms show an asymmetric shape, leveling off at lower temperatures. At these temperatures, the densities of excited ν_{CO} and ν_3 become so small, that the remaining transmittance peaks are not distinguishable from noise. In Fig. 5 this explains T_{CO} being fitted too low before the plasma pulse and after 7.00 ms.

Furthermore, the width of the parabola shape can be used as an indication for the sensitivity of the fitted transmittance to a particular parameter. T_{rot} and $T_{1,2}$ show equally sharp shapes with an average half width at $\chi^2_{\mathrm{red}} = \chi^2_{\mathrm{red,\,min}}+0.5$ of 30 K and 27 K, respectively. The shapes of T_3 are with a half width of 67 K twice as broad, while those of T_{CO} are by far widest at 357 K. A variation in the measured transmittance (e.g. resulting from a fluctuation in the plasma conditions of the emission background with respect to the normal transmission measurement, see section 2) is therefore likely to cause largest deviations in the fitted T_{CO}.

4.3. Influence of initial gas mixtures

To further discuss the temperature development during the plasma cycle, the fitting results of different cycles are compared in Fig. 7. During the 5-10 ms on-off pulse in panel (a), a molecule experiences on average ca. 150 discharges before leaving the reactor. The fitted conversion is $\alpha = 0.18$, resulting in a mixture of 75.2% CO_2, 16.5% CO, and 8.3% O_2 (see Eqs. (6) and (7)). In contrast to this, in panel (b) the fit outcome of a measurement is shown where a molecule sees only one plasma pulse. To achieve this, the flow rate is increased from 7.4 sccm to 166 sccm of CO_2 while the plasma-off time is increased to 150 ms. Now, the residence time of the gas of ca. 100 ms is well below the off time, purging the reactor of most CO and O_2 before the next discharge. Accordingly, this measurement is referred to as the single-pulse measurement. It should be noted that the conversion during a single discharge is not enough to be able to accurately fit α or T_{CO}.

Practically, due to the longer plasma-off time, the measurement time increases from the regular two times 2 hours (transmission and emission measurement) to two times 10 hours, which makes it challenging to maintain constant discharge conditions and IR detector temperature. Further increasing the flow rate reduces the required off time and therefore the measurement time, but would also increase the renewal of the gas during the discharge, which is already 5%. The injection of thermal gas in an ongoing discharge is likely to influence the temperature dynamics and should therefore be minimized.

Comparing the graphs in Fig. 7(a) and (b), the development of temperatures over time is similar: when the plasma turns on, T_3 rapidly increases with a maximum around 0.7 ms, after which T_{rot} and $T_{1,2}$ increase and all temperatures level off in a non-thermal equilibrium. The temperatures quickly thermalize after plasma-off, which takes somewhat longer in the single-pulse measurement. The difference in absolute values of the temperatures between (a) and (b) is to a large extent explained by the lower initial temperatures, resulting from a full renewal with cold gas before the next pulse. Furthermore, during the single pulse the temperatures show irregularities, best visible between 2 ms and 5 ms, which result from variations between single discharges. When the plasma-off time is small, discharges ignite more stable. Other differences, such as the increased $T_{1,2}$ between 0 ms and 2 ms, are attributed to the absence of interactions of CO_2 with CO or O_2, this being the prominent difference between the plasma conditions.

4.4. Excitation of the asymmetric stretch mode

Focussing on the excitation of the asymmetric stretch vibration of CO_2, potentially relevant for an efficient dissociation, it is examined whether an elevated T_3 is typical for the start of a discharge. To do so, Fig. 7(c) shows the result of a measurement where the 5-10 ms on-off pulse is preceded by a 0.75-0.75 ms on-off pre-pulse. The temperature development during the pre-pulse matches the first 0.75 ms in the pulse of panel (a). At the start of the 5 ms pulse, T_3 peaks again, but reaches a lower maximum. The pulse continues comparable to the

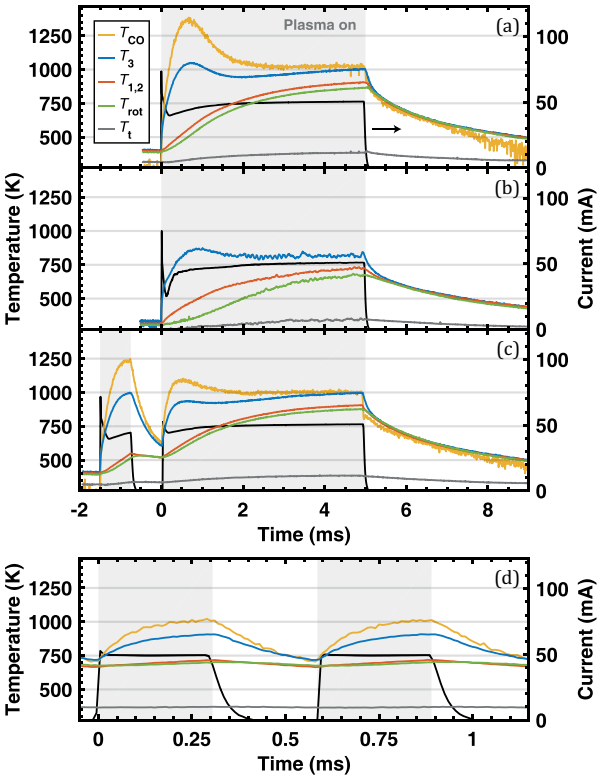

Fig. 7: Four time-resolved measurement series at a pressure of 6.7 mbar and plasma current of 50 mA. The plasma current and fitted temperatures are plotted versus time. (a): 5-10 ms on-off measurement, same as in Fig. 5. (b): Single-pulse measurement, in which the off-time is increased to 150 ms to remove all CO and O_2 before the next discharge. (c): 0.75-0.75-5-10 ms on-off-on-off measurement. The same as (a), but with a 0.75-0.75 ms on-off pre-pulse. (d): 0.3-0.3 ms on-off (two periods are shown).

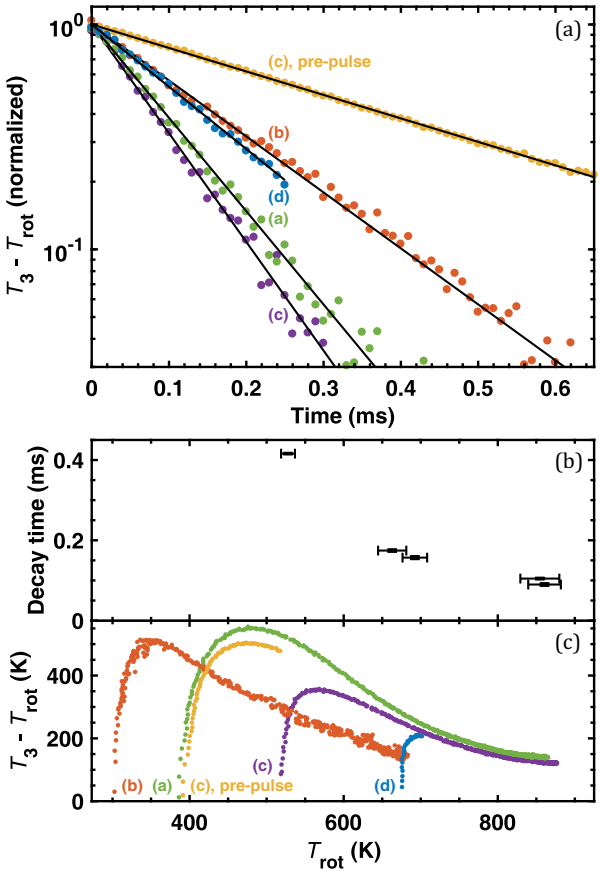

Fig. 8: (a) Normalized relaxation of T_3 to T_{rot} versus time after plasma off. The labels correspond to the panel labels of Fig. 7. The black solid lines represent the fitted exponential decay. (b) The characteristic decay times versus the rotational temperature during relaxation. (c) The elevation of T_3 with respect to T_{rot} versus the rotational temperature, during the plasma-on phases of Fig. 7.

one in panel (a). After the pre-pulse, the relaxation of T_3 to T_{rot} takes longer than at the end of the 5 ms plasma pulse and when after 0.75 ms the 5 ms pulse starts, T_3 is not fully relaxed yet.

Based on this, it is examined whether a repeating rapid excitation with an incomplete relaxation can lead to further elevation of T_3. To this purpose, the results of an on-off cycle of 0.3-0.3 ms is shown in Fig. 7(d). From the graph it can be seen that T_3 never completely relaxes, but its maximum excitation is not higher than for the other cycles. Besides, T_{rot} and $T_{1,2}$ stay relatively high and constant between 650 K and 725 K. T_3 relaxation after the pulse takes place with a similar speed as for the single pulse in panel (b).

To quantify the relaxation of T_3 to T_{rot} for all panels of Fig. 7, the difference between these two temperatures after plasma off is fitted with a single exponential decay. The relaxation after the pre-pulse in panel (c) is fitted as well. The results are shown on a logarithmic scale and normalized to the initial temperature difference in Fig. 8(a). The labels of the data correspond to the panels of Fig. 7. The fitted exponential curves are presented as solid black lines and are in good agreement with the data.

The different slopes show that the characteristic decay time varies strongly between data sets. While most experimental conditions during these plasma-off phases are similar, the rotational or translational temperature ranges from 530 K during the pre-pulse relaxation (c) to 860 K during the relaxation of (a) and (c). Fig. 8(b) shows the fitted characteristic times versus the rotational temperature during the relaxation. Since T_{rot} varies over time, the decay time is plotted versus the average rotational temperature during a time period of twice the fitted characteristic decay time. The horizontal error bars represent twice the standard deviation of T_{rot} over this same period. The graph indicates a strong decrease of the decay time with increasing rotational temperature. This agrees with increasing rate constants for ν_3 relaxation with increasing translational temperature [41, 42].

The rotational temperature dependence of T_3 relaxation to T_{rot} should be apparent in the plasma-on phase as well. To illustrate this, panel (c) of Fig. 8 shows $T_3 - T_{rot}$ during the discharges of Fig. 7 versus the rotational temperature. All graphs develop similarly towards an equilibrium between relaxation and excitation, e.g. by electron impact, starting with a rapid increase at low T_{rot} when the discharge ignites. After reaching equilibrium around the maximum, the equilibrium temperature gradually decreases with increasing T_{rot}. The rotational temperature dependence of this decrease is proportional to the one of the T_3 to T_{rot} decay time in Fig. 8(b). This illustrates the influence of translational temperature dependent relaxation on the T_3 elevation during a discharge.

The fact that the single-pulse measurement (b) shows the same development, but does not align with the rest, can be explained by the absence of CO for the single pulse versus a fitted 16.5%, 17.7%, and 22.0% of CO for (a), (c), and (d), respectively. It is known from literature that CO can stimulate vibrational excitation of the asymmetric stretch mode of CO_2 [22]. Therefore, a CO stimulated excitation increase for pulses (a), (c), and (d) results in a higher equilibrium temperature for T_3.

5. Conclusions

We have demonstrated a method to determine elevated vibrational temperatures of CO_2 and CO in a glow discharge in a time-resolved way, using *in situ* Fourier transform infrared spectroscopy. An algorithm is developed to analyze the measured transmittance spectra. As the outer ends of the reactor are filled with gas at a temperature colder than the gas in the discharge, a thermal-volume fraction is introduced in the model. The algorithm has been used to fit a previously published CO_2 spectrum, showing highly vibrationally excited CO_2 transitions. There is a very good agreement between fit and data.

To study the influence of the initial gas mixture, a measurement where the gas residence time is much longer than the plasma period is compared to one where the gas is fully renewed between two pulses. Both show a qualitatively similar development of temperatures over time. Absolute differences are attributed to the significantly increased presence of CO and O_2 in the multiple-pulse measurement in regard to the single-pulse measurement. Due to the shorter plasma-off time of the multiple-pulse measurement, the discharge ignites in a more stable and consistent way.

It is experimentally shown that the temperature dependence of T_3 relaxation is likely to be the leading mechanism for the decrease of T_3 elevation with increasing T_{rot}. The T_3 peak found at the start of a sufficiently long plasma pulse is therefore not so much a consequence of a starting discharge, but is caused by a low T_{rot}. Hence, to gain higher excitations of the asymmetric stretch mode, potentially relevant for the efficient dissociation of CO_2, relaxation could be strongly impeded by keeping the gas temperature low.

Acknowledgements

This work is partially funded by the Netherlands Organisation for Scientific Research (NWO), under reference 713.013.003, and partially by LABEX Plas@par receiving financial aid managed by the French National Research Agency (ANR) under the references ANR-11-IDEX-0004-0, and ANR-16-CE06-0005.

References

[1] Centi G, Quadrelli E A and Perathoner S 2013 *Energy & Environmental Science* **6** 1711 ISSN 1754-5692 URL http://xlink.rsc.org/?DOI=c3ee00056g

[2] van Rooij G J, van den Bekerom D C M, den Harder N, Minea T, Berden G, Bongers W A, Engeln R, Graswinckel M F, Zoethout E and van de Sanden M C M 2015 *Faraday Discuss.* **183** 233–248 ISSN 1359-6640 URL http://xlink.rsc.org/?DOI=C5FD00045A

[3] Bogaerts A, Kozák T, van Laer K and Snoeckx R 2015 *Faraday Discuss.* **183** 217–232 ISSN 1359-6640 URL http://xlink.rsc.org/?DOI=C5FD00053J

[4] Brehmer F, Welzel S, van de Sanden M C M and Engeln R 2014 *Journal of Applied Physics* **116** 123303 ISSN 0021-8979 URL http://aip.scitation.org/doi/10.1063/1.4896132

[5] Capezzuto P, Cramarossa F, D'Agostino R and Molinari E 1976 *The Journal of Physical Chemistry* **80** 882–888 ISSN 0022-3654 URL http://pubs.acs.org/doi/abs/10.1021/j100549a024

[6] Legasov V A, Zhivotov V K, Krasheninnikov E G, Krotov M F, Patrushev L, Rusanov V D, Rykunov G V, Spektor A M, Fridman A A and Sholin G V 1978 *Soviet Physics Doklady* **238** 66–69

[7] Fridman A 2008 *Plasma Chemistry* (New York: Cambridge University Press) ISBN 9780521847353

[8] Siemsen K, Reid J and Dang C 1980 *IEEE Journal of Quantum Electronics* **16** 668–676 ISSN 0018-9197 URL http://ieeexplore.ieee.org/document/1070536/

[9] Dang C, Reid J and Garside B K 1982 *Applied Physics B Photophysics and Laser Chemistry* **27** 145–151 ISSN 0721-7269 URL http://link.springer.com/10.1007/BF00694640

[10] Andreev S and Savinov S 1995 *Bulletin of the Lebedev Physics Institute* **6** 26–30

[11] Andreev S, Zakharov V, Ochkin V and Savinov S 2004 *Spectrochimica Acta Part A: Molecular and Biomolecular Spectroscopy* **60** 3361–3369 ISSN 13861425 URL http://linkinghub.elsevier.com/retrieve/pii/S1386142504001143

[12] Rivallan M, Aiello S and Thibault-Starzyk F 2010 *Review of Scientific Instruments* **81** 103111 ISSN 00346748 URL http://scitation.aip.org/content/aip/journal/rsi/81/10/10.1063/1.3492094

[13] Plönjes E, Palm P, Lee W, D Chidley M, Adamovich I V, R Lempert W and Rich J 2000 *Chemical Physics* **260** 353–366 ISSN 03010104 URL http://linkinghub.elsevier.com/retrieve/pii/S0301010400002573

[14] Lee W, Adamovich I V and Lempert W R 2001 *The Journal of Chemical Physics* **114** 1178–1186 ISSN 0021-9606 URL http://aip.scitation.org/doi/10.1063/1.1332400

[15] Doerk T, Ehlbeck J, Jauernik P, Stańco J, Uhlenbusch J and Wottka T 1992 *Il Nuovo Cimento D* **14** 1051–1063 ISSN 0392-6737 URL http://link.springer.com/10.1007/BF02455367

[16] Kishimoto T, Wenzel N and Grosse-Wilde H 1992 *Spectrochimica Acta Part B: Atomic Spectroscopy* **47** 51–60 ISSN 05848547 URL http://linkinghub.elsevier.com/retrieve/pii/0584854792800052

[17] Shimanouchi T 1972 Tables of molecular vibrational frequencies, consolidated volume 1 Tech. rep. National Bureau of Standards Gaithersburg, MD URL http://dx.doi.org/10.6028/NBS.NSRDS.39

[18] Depraz S, Perrin M and Soufiani A 2012 *Journal of Quantitative Spectroscopy and Radiative Transfer* **113** 1–13 ISSN 00224073 URL http://dx.doi.org/10.1016/j.jqsrt.2011.09.002

[19] Depraz S, Perrin M, Rivière P and Soufiani A 2012 *Journal of Quantitative Spectroscopy and Radiative Transfer* **113** 14–25 ISSN 00224073 URL http://linkinghub.elsevier.com/retrieve/pii/S0022407311003359

[20] Welzel S, Hempel F, Hübner M, Lang N, Davies P B and Röpcke J 2010 *Sensors* **10** 6861–6900 ISSN 1424-8220 URL http://www.mdpi.com/1424-8220/10/7/6861/

[21] Raizer Y P 1991 *Gas Discharge Physics* (Berlin, Heidelberg: Springer-Verlag) ISBN 3-540-19462-2

[22] Witteman W J 1987 *The CO_2 Laser* (Berlin, Heidelberg: Springer-Verlag) ISBN 3540176578

[23] Suzuki I 1968 *Journal of Molecular Spectroscopy* **25** 479–500 ISSN 00222852 URL http://www.sciencedirect.com/science/article/pii/S0022285268800189

[24] Amat G and Pimbert M 1965 *Journal of Molecular Spectroscopy* **16** 278–290 ISSN 0022-2852 URL http://www.sciencedirect.com/science/article/pii/0022285265901232

[25] Rothman L, Gordon I, Barber R, Dothe H, Gamache R, Goldman A, Perevalov V, Tashkun S and Tennyson J 2010 *Journal of Quantitative Spectroscopy and Radiative Transfer* **111** 2139–2150 ISSN 00224073 URL http://dx.doi.org/10.1016/j.jqsrt.2010.05.001

[26] Huber K P, Herzberg G, Gallagher J W and Johnson III R D 2016 Constants of Diatomic Molecules *NIST Chemistry WebBook, NIST Standard Reference Database Number 69* ed Linstrom P J and Mallard W G (Gaithersburg MD: National Institute of Standards and Technology) URL http://webbook.nist.gov

[27] Fischer J, Gamache R, Goldman A, Rothman L and Perrin A 2003 *Journal of Quantitative Spectroscopy and Radiative Transfer* **82** 401–412 ISSN 00224073 URL http://linkinghub.elsevier.com/retrieve/pii/S0022407303001663

[28] Herzberg G 1960 *Molecular spectra and molecular structure II. Infrared and Raman spectra of polyatomic molecules* 9th ed (London: Van Nostrand) ISBN 9780442033866

[29] Hoskins L C 1975 *Journal of Chemical Education* **52** 568 ISSN 0021-9584 URL http://pubs.acs.org/doi/abs/10.1021/ed052p568

[30] Šimečková M, Jacquemart D, Rothman L S, Gamache R R and Goldman A 2006 *Journal of Quantitative Spectroscopy and Radiative Transfer* **98** 130–155 ISSN 00224073 URL http://linkinghub.elsevier.com/retrieve/pii/S0022407305002931

[31] McDowell R S 1988 *The Journal of Chemical Physics* **88** 356 ISSN 00219606 URL http://aip.scitation.org/doi/10.1063/1.454608

[32] Mantz A, Maillard J P, Roh W B and Narahari Rao K 1975 *Journal of Molecular Spectroscopy* **57** 155–159 ISSN 00222852 URL http://linkinghub.elsevier.com/retrieve/pii/0022285275900491

[33] Chen D W, Narahari Rao K and McDowell R S 1976 *Journal of Molecular Spectroscopy* **61** 71–78 ISSN 00222852 URL http://linkinghub.elsevier.com/retrieve/pii/0022285276903817

[34] Treanor C E 1968 *The Journal of Chemical Physics* **48** 1798 ISSN 00219606 URL http://scitation.aip.org/content/aip/journal/jcp/48/4/10.1063/1.1668914

[35] Gamache R R and Rothman L S 1992 *Journal of Quantitative Spectroscopy and Radiative Transfer* **48** 519–525 ISSN 00224073 URL http://linkinghub.elsevier.com/retrieve/pii/002240739290117M

[36] Rothman L, Rinsland C, Goldman A, Massie S, Edwards D, Flaud J M, Perrin A, Camy-Peyret C, Dana V, Mandin J Y, Schroeder J, McCann A, Gamache R, Wattson R, Yoshino K, Chance K, Jucks K, Brown L, Nemtchinov V and Varanasi P 1998 *Journal of Quantitative Spectroscopy and Radiative Transfer* **60** 665–710 ISSN 00224073 URL http://linkinghub.elsevier.com/retrieve/pii/S0022407398000788

[37] Gharavi M and Buckley S G 2004 *Applied Spectroscopy* **58** 468–473 ISSN 00037028 URL http://as.osa.org/abstract.cfm?URI=as-58-4-468

[38] Whiting E 1968 *Journal of Quantitative Spectroscopy and Radiative Transfer* **8** 1379–1384 ISSN 00224073 URL http://linkinghub.elsevier.com/retrieve/pii/0022407368900812

[39] Nuttall A 1981 *IEEE Transactions on Acoustics, Speech, and Signal Processing* **29** 84–91 ISSN 0096-3518 URL http://ieeexplore.ieee.org/document/1163506/

[40] Drosg M 2009 *Dealing with Uncertainties* 2nd ed (Berlin, Heidelberg: Springer Berlin Heidelberg) ISBN 978-3-642-01383-6 URL http://link.springer.com/10.1007/978-3-642-01384-3

[41] Blauer J A and Nickerson G R 1973 A survey of vibrational relaxation rate data for processes important to CO_2-N_2-H_2O infrared plume radiation Tech. Rep. AFRPL-TR-73-57 Ultrasystems, Inc. URL http://www.dtic.mil/dtic/tr/fulltext/u2/771554.pdf

[42] Kozák T and Bogaerts A 2014 *Plasma Sources Science and Technology* **23** 045004 ISSN 0963-0252 URL http://stacks.iop.org/0963-0252/23/i=4/a=045004?key=crossref.ae2245ca0b3f38b3e8652fc96aea2549